JPE 16-2-1

http://dx.doi.org/10.6113/JPE.2016.16.2.399
ISSN(Print): 1598-2092 / ISSN(Online): 2093-4718

A Modular Bi-Directional Power Electronic Transformer

Zhigang Gao† and Hui Fan*

†,*School of Automation, Beijing Institute of Technology, Beijing, China

Abstract

This paper presents a topology for a modular power electronic transformer (PET) and a control scheme. The proposed PET consists of a cascaded H-Bridge rectifier on the primary side, a high-frequency DC/DC conversion cell in the center, and a cascaded H-Bridge inverter on the secondary side. It is practical to use PETs in power systems to reduce the cost, weight and size. A detailed analysis of the structure is carried out by using equivalent circuit. An algorithm to control the voltages of each capacitor and to maintain the power flow in the PET is established. The merits are analyzed and verified in theory, including the bi-directional power flow, variable voltage/frequency and high power factor on the primary side. The experimental results validated the propose structure and algorithm.

Key words: Bi-directional, Cascaded H-Bridge (CHB), Multilevel converter, Power Electronic Transformer (PET), Pulse Width Modulation (PWM)

I. INTRODUCTION

Due to the requirements of modern power systems and electric drives, more and more power electronic devices are being applied to improve the reliability, increase the power factor and optimize the power flow [1]-[5]. At present, it is possible to replace the traditional line-frequency (LF) transformers [6]-[8], which are usually employed for power conversion, with high-frequency (HF) transformers and power electronic devices in several applications.

Unlike LF transformers, this new kind of power conversion system consists of two kinds of elements, which are HF-transformers and power electronic devices. In addition, it is called a power electronic transformer (PET), also referred to as a solid-state transformer [9]-[10]. Compared with traditional transformers, the PET has many advantages such as small size, high power density, simple monitoring and control. In addition, since the PET is an active transformer, it has the capability of regulating voltage and power in a wide range.

Fig.1 shows a comparative photo of 50Hz LF and 20kHz HF transformers. The HF transformer has a low volume, light weight and low cost. As a key part of a PET, the HF transformer usually has two functions. These functions are (1) isolation and (2) energy transfer.

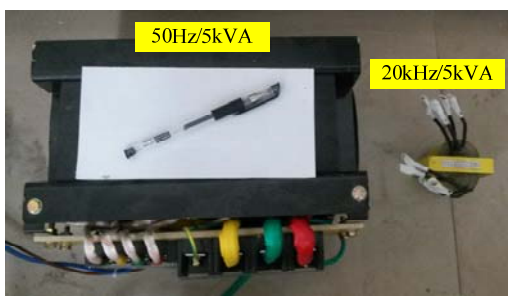

Fig. 1. Comparative photo of 50Hz LF and 20kHz HF transformers.

Fig. 2 shows a diagram of the PET. Typically, the converters in a PET can be divided into two groups: grid-side and transformer-side. The grid-side converters can implement AC/DC or DC/AC conversions, while the transformer-side converters can generate HF voltages and control the power flowing through HF transformers [11]-[15]. Generally speaking, most power electronic converters can meet these requirements, such as fly-back, push-pull, half-bridge and full-bridge. The authors of [16] described the advantages of a full-bridge topology and explained that it can be the core circuit for the next generation of power conversion systems.

Manuscript received May 7, 2015; accepted Sep.16, 2015
Recommended for publication by Associate Editor Honnyong Cha.
†Corresponding Author: gzg@bit.edu.cn
Tel: +86-13466772534, Beijing Inst. of Tech.
*School of Automation, Beijing Institute of Technology, China

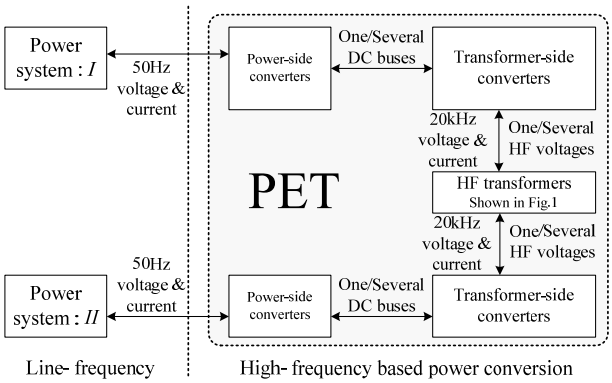

Fig. 2. Diagram of PET.

This viewpoint has been accepted by many researchers. In addition, relative studies on the subject have been reported [17]-[22]. These studies are about the circuit performance, control scheme, hardware design, modulation method and optimization.

Many applications for PETs in power systems have been reported [23]-[25]. However, less attention has been paid to the structure or topology of PETs, especially for high voltage applications.

Multilevel topologies have gained more attention due to their advantages in terms of high voltage, large volume, high power quality, low switching losses and low harmonic issues [26]-[31]. Thus, it is practical to develop high voltage power electronic transformers that connect the generation and the consumption in power systems.

In power systems, the transformer changes the amplitude of voltage from one level to another. In China, the typical rating voltages (RMS value) are 6kV, 10kV, 35kV, 110kV, etc. In wind power generation farms, the voltage is 690V/3-Φ, and the electric trains in China are powered by 25kV/1-Φ.

Overall, there are three requirements for PETs, as discussed below.

A. High voltage.

Due to the limitations of power electronic devices, it is not possible to do direct power conversion in high voltage occasions. Multilevel converters make it practical to form a high voltage converter with low voltage rating power electronic devices. Multilevel converters were first proposed in the last century and have been widely used in a lot of applications, such as compressors, mixers, fans, reactive power compensation, railway traction, wind power generation, and power systems [32]-[34]. At this point, a lot of topologies have been proposed, such as neutral point clamped, cascaded H-Bridge and flying capacitors [35]-[39].

For 10kV or even higher voltage levels, the CHB converters, which were first proposed in 1975 [40], are considered to be reasonable and practical because of their modularity and simplicity. The CHB is attractive due to its modular topology and high reliability because each switch is clamped by the capacitor, the voltage of which can be controlled as a constant voltage source. Moreover, extra clamping diodes and capacitors, which are necessary in other topologies, are not required [41]. The principles of conventional CHB converters are discussed in [42]-[46]. By shifting the phase of the carrier, the switching frequency harmonics can be moved to the higher frequency side.

B. Bi-directional power flow.

Bi-directional power flow is necessary for PETs to connect two power grids together. However, the diode rectifier in the CHB converter prevents the power from flowing bi-directionally.

A bi-directional cascaded H-Bridge converter is proposed in [47], where the diode rectifiers are replaced with three phase PWM rectifiers. However, the bulky and expensive LF transformer still exists. Similar topologies were presented in [48], where PWM rectifiers with one or two arms are adopted. A direct back to back CHB converter has also been presented. The structure was simplified and the power can flow bi-directionally. However, because each DC capacitor is connected to two H-Bridges, the system has many faulty states as described in [49]. A multilevel rectifier based on H-Bridges was established in [50], where the CHB operated as a rectifier. The control algorithm was complex and the system can become unsteady in certain cases.

C. Low Size, Weight and Cost

The phase-shifting LF transformer is of great size, weight and cost in converter systems [51][52]. With the development of semi-conductor technologies, the cost of power electronic devices will become lower and lower. In the literatures, many topologies and techniques based on the H-Bridge discussed the elimination of the low frequency transformer [53]-[56].

With the development of new magnetic materials such as FINEMET, high frequency isolation techniques have received more attention because of their low price, small size, high efficiency and an improved energy density [57][58].

This paper is organized as follows. The proposed topology for a PET is discussed in section II. The control algorithm of the PET, including the three parts shown in Fig. 3, is discussed in section III. Experimental results, which validate the proposed functions in this paper, are introduced in section IV. Some conclusions are given in section V.

II. PROPOSED TOPOLOGY OF A PET

This paper proposed a CHB based bi-directional topology to form a PET, as shown in Fig. 3. The proposed PET mainly consists of three parts which are a CHB rectifier, a DC/DC conversion and an inverter.

The left side in Fig. 3 is referred to as the primary side, and the right side is referred to as the secondary side. The proposed topology has many advantages in high voltage, high

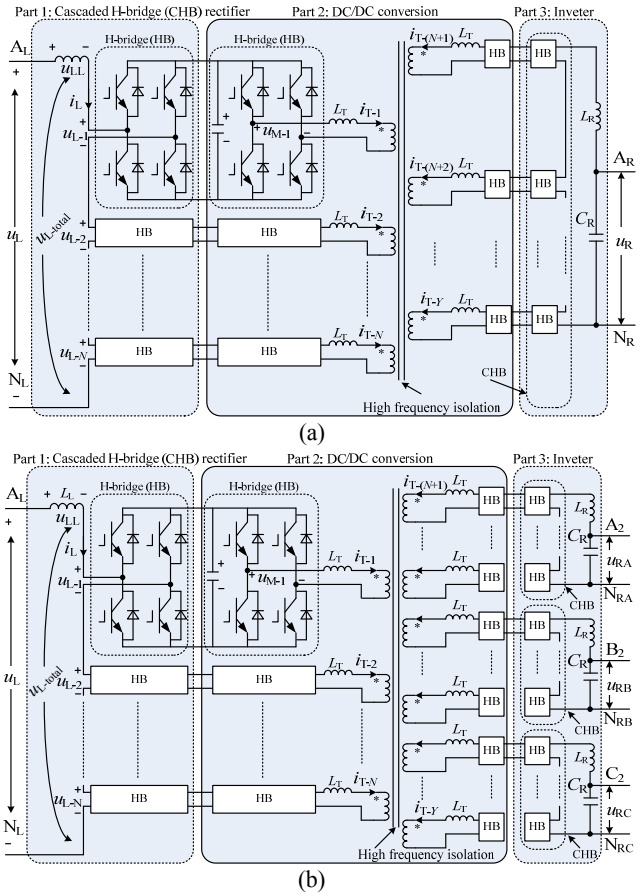

Fig. 3. Proposed PET topology. (a) Single-phase-in/ single-phase-out application. (b) Single-phase-in/ three-phase-out application.

power density and high efficiency applications.

With proper control schemes, DC voltages can be maintained and a bi-directional power flow can be achieved. The DC sources on the secondary side are isolated with each other so that they can be connected with separate inverters and serialized together to generate high voltages. In addition, this topology can be extended to multi-phase applications, which may be useful in specific power systems.

The left side in Fig. 3 is referred to as the primary side, while the right side is referred to as the secondary side. The proposed topology has many advantages in high voltage, high power density and high efficiency applications.

With proper control schemes, DC voltages can be maintained and a bi-directional power flow can be achieved. The DC sources on the secondary side are isolated from each other so that they can be connected with separate inverters and serialized together to generate high voltages. In addition, this topology can be extended to multi-phase applications, which may be useful in specific power systems.

Fig. 4 shows an application of a PET. The PET works as a junction for different types of power systems, which are single-phase and three-phase power systems in this case.

As shown in Fig.3, the DC capacitor voltages of the CHB

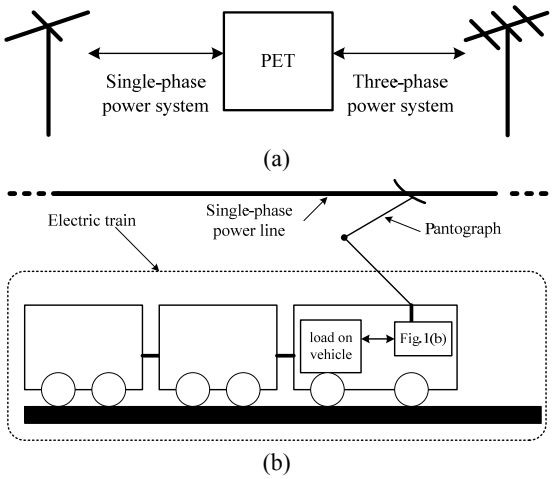

Fig. 4. Possible applications for single-phase-in/three-phase-out topology. (a) Junction for different types of power systems. (b) As three-phase power supply with reduced height and weight for electric vehicles.

rectifier are denoted as $U_{dc\text{-}1}$, $U_{dc\text{-}2}$, … , and $U_{dc\text{-}N}$. The grid voltage on the primary side is u_L and the input current is i_L. The voltage on the inductor L_L on the primary side is u_{LL}. The input voltages of each H-Bridge in the CHB rectifier are referred to as $u_{L\text{-}1}$, $u_{L\text{-}2}$, ... , and $u_{L\text{-}N}$.

The output voltages of the H-Bridges, denoted as $u_{M\text{-}1}$, $u_{M\text{-}2}$, ... , and $u_{M\text{-}N}$, are connected to the windings of a HF transformer. The currents flowing into the wings are referred to as $i_{T\text{-}1}$, $i_{T\text{-}2}$, ... , and $i_{T\text{-}N}$. The leakage inductors of the windings are assumed to be equal and are denoted as L_T for the sake of simplicity.

Some features of the PET shown in Fig. 3 can be concluded as follows.

1) High voltage is available. Each side of the topology is based on a CHB. Therefore, by increasing the number of the H-Bridges, a high voltage can be obtained. As a result, the PET can be directly connected to high voltage power systems to replace traditional LF transformers.

2) Flexibility for power system operation. It is well know that traditional transformers have a limited ability to change the turn ratio for voltage regulation. On the other hand, a PET can change the frequency and amplitude of the voltage. Therefore, it provides a flexible way for power system to operate, especially in terms of voltage regulation and power maintenance.

3) High Modularization. A PET consists of a certain number of H-Bridges, whose parameters are the same. Therefore, it is highly modularized and a faulty H-Bridge can be easily replaced.

4) Power factor correction. A PET can improve the power factor on the primary side. In addition, the power factor can be as high as 1, which will lower the cost of the power line and increase the efficiency.

5) Bi-directional power flow. Due to this, a PET can allow two power systems to exchange energy.

6) Low size and high power density. High-frequency techniques are adopted to reduce the size of the materials.

III. CONTROL ALGORITHM

A. CHB Rectifier

1) Control of the Active Power

A CHB rectifier operates to keep the sum of all the capacitor voltages constant, and the DC/DC conversion is introduced to keep all of the capacitor voltages equal (as discussed in sub-section B, section III). The input current is sinusoidal to eliminate harmonics. The power factor can be maintained as high as 1 to eliminate the reactive power on the primary side.

The equivalent circuit of the CHB rectifier is introduced in [60], and it is used to analyze the steady state characteristics of the rectifier. $\mathbf{U_L}$, $\mathbf{I_L}$, $\mathbf{U_{LL}}$ and $\mathbf{U_{L\text{-}total}}$ are the vectors of u_L, i_L, u_{LL} and $u_{L\text{-}total}$ shown in Fig. 3.

The equivalent circuit, discussed in [60], consists of two sinusoidal voltage sources and an inductor. As a result, it can be analyzed by using a vector diagram. $\mathbf{U_L}$ is ahead of $\mathbf{I_L}$ by β. The active power P_L flowing into the rectifier under sinusoidal conditions can be written as (1).

$$P_L = |\mathbf{U_L}||\mathbf{I_L}|\cos(\beta)/2 \tag{1}$$

As depicted in Fig. 5, the reference value of i_L (denoted by i_L^*) can be obtained by timing the output of the DC voltage loop and the grid voltage u_L. A PI regulator is adopted in the DC voltage loop. However, in the grid current loop, since i_L^* is sinusoidal, a Proportional-Resonant (PR) regulator is used.

2) Current Regulator in the Rectifier

A PR regulator is introduced to trace the sinusoidal signal, as discussed in [59], [60]. As shown in Fig. 5, i_L is sinusoidal (50Hz) and it is practical to track it with a PR regulator (the resonant angular frequency is $2\pi\times50=100\pi$ rad/second).

$$L_L\frac{di_L}{dt} = u_L - u_{L\text{-total}} \tag{2}$$

Fig. 6 shows the details of the current-loop regulator in the rectifier. G(s) is the transfer function, and the expression is shown further in Fig. 6(b). $1/(s+T_s)$ is the delay caused by the PWM. T_s=0.5ms (the switching frequency of the rectifier is 2kHz, as shown in section IV) is the sample period of the rectifier. $1/L_Ls$ is the transfer function of the inductor, and L_L=1mH. Fig. 6(b) shows the structure of the regulator. In Fig. 6(c), the system is divided into two parts, in which the regulators are K_P and $K_Rs/(s^2+\omega_0^2)$, respectively. ω_0 is the resonant angular frequency of the regulator. In China, $\omega_0=100\pi$(rad/s), since the power grid frequency is 50Hz.

The open-loop transfer function for part-1 in Fig. 6(c) can be written as (3), which is a typical I-type transfer function. Based on the theory of automatic control, let K_PT_s/L_L=0.5. Thus, K_P can be calculated as (4).

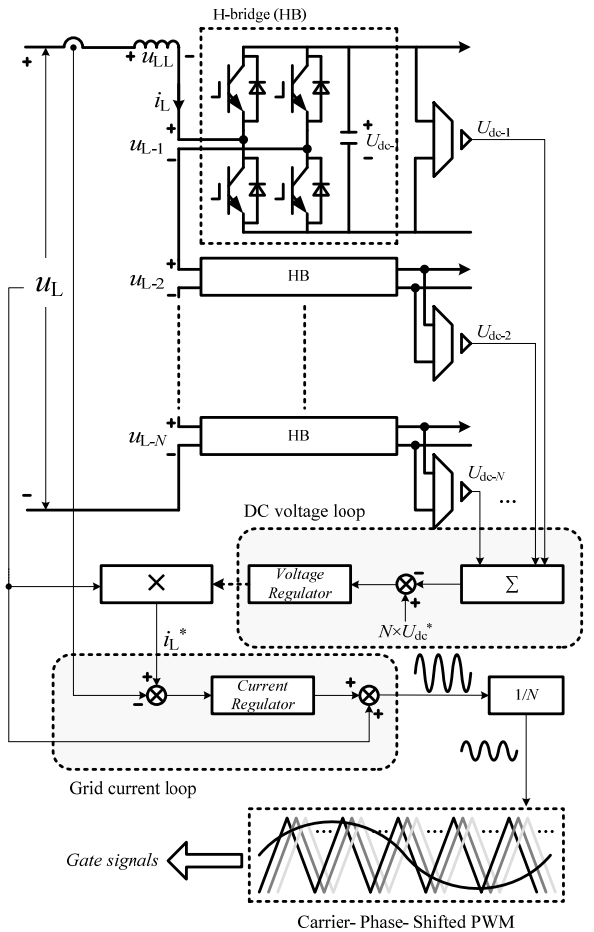

Fig. 5. Control scheme for CHB rectifier.

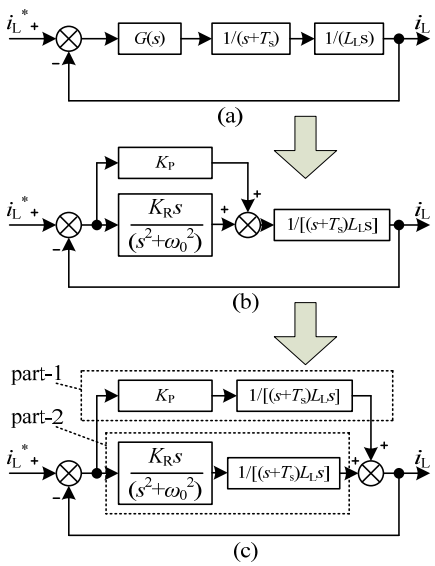

Fig. 6. Current loop based on PR regulator. (a) Diagram of current loop. (b) Control loop with PR regulator. (c) Two parts for the PR regulator in the control loop.

$$G_{\text{part-1}}(s) = \frac{K_P}{s(s+T_s)L_L} \tag{3}$$

$$\frac{K_{\mathrm{P}}}{L_{\mathrm{L}}}T_{\mathrm{s}}=0.5\Rightarrow K_{\mathrm{P}}=\frac{0.5L_{\mathrm{L}}}{T_{\mathrm{s}}}=1 \tag{4}$$

The open-loop transfer function for part-2 in Fig. 6(c) can be written as (5).

$$G_{\mathrm{part-2}}(s)=\frac{K_{\mathrm{R}}}{(s^2+\omega_0^2)(s+T_{\mathrm{s}})L_{\mathrm{L}}} \tag{5}$$

Therefore, the following is obtained:

$$G_{\mathrm{part-2}}(\omega j)=\frac{\frac{K_{\mathrm{R}}}{L}}{T_{\mathrm{s}}(\omega_0^2-\omega^2)+\omega(\omega_0^2-\omega^2)j} \tag{6}$$

The power grid frequency is not constant, and the frequency error Δf is usually about 0.01~0.1Hz. The gain was set to be 10 or more to assure the performance of the system. Thus, the following is obtained:

$$\begin{cases}\left|G_{\mathrm{part-2}}(\omega j)\right|=10 \text{ when } \Delta f=0.01 \Rightarrow K_{\mathrm{R}}=124\\ \left|G_{\mathrm{part-2}}(\omega j)\right|=10 \text{ when } \Delta f=0.1 \Rightarrow K_{\mathrm{R}}=1240\end{cases} \tag{7}$$

It should be noted that K_{R} cannot be too large. If it is, higher current ripples on the inductor will be induced. In addition, the parameters need tuning in practical applications.

In this paper, K_{R} was set to 1000. This is considered as a compromise in (7). In addition, K_{P} was set to 1, as shown in (4). The system performance is validated in section IV.

Therefore, the open-loop transfer function is:

$$F_{ol}(s)=\frac{10^3}{s(s+0.0005)}+\frac{10^6}{(s^2+\omega_0^2)(s+0.0005)} \tag{8}$$

Fig. 7 shows the open-loop gain in Fig. 6(c), in which L_{L}=1mH, K_{p}=1, and K_{R}=1000. The gain at 50Hz is large enough, which leads to a high trace precision for the reference value i_{L}^*.

When the gain is 0dB, the phase of the transfer function is calculated in (8), and it is -161° (larger than -180°). Hence, the stability can be verified.

As shown in Fig. 5, the carrier phases of each H-Bridge are shifted by π/N to eliminate harmonics. Thus, the gate signals of all the H-Bridges are not the same.

It is important to indicate that the load of each H-Bridge may not be exactly the same. Because of the differences between the carrier phases, the power flowing into each H-Bridge is not equal. Therefore, the capacitor voltages can hardly be kept the same without special capacitor voltage balancing algorithms. In this paper, the DC/DC conversion shown in Fig. 5 aims to keep all of the capacitor voltages the same by adjusting the power flowing into the windings of the HF transformer. In that case, all of the DC voltages can be kept the same as the desired value.

B. DC/DC Conversion

1) Power Model of the DC/DC Conversion

As shown in Fig. 3, there is a HF transformer in the center of the DC/DC conversion. The turn ratio of every two windings is 1. In addition, the parameters of every two

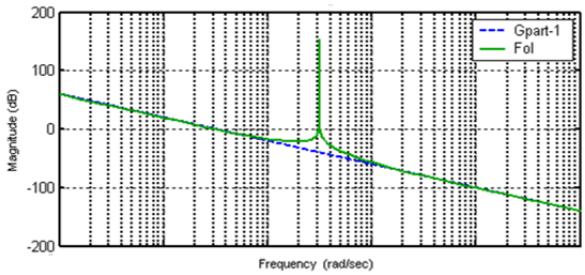

Fig. 7. Open-loop gains for CHB rectifier.

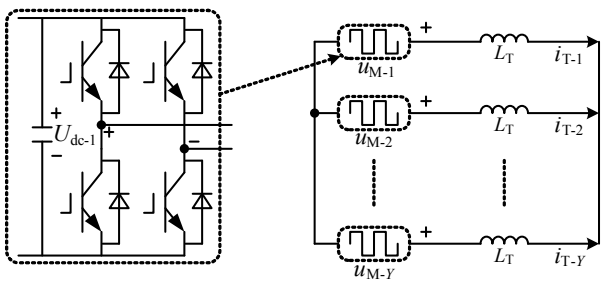

Fig. 8. Equivalent circuit of DC/DC conversion.

H-Bridges are the same.

The number of the windings is designed to meet specific requirements. It depends on the number of H-Bridges. In Fig. 3, the total number of the windings is Y, N of which are connected with the H-Bridge rectifier.

The objective of the DC/DC conversion is to keep all of the DC voltages the same as $U_{\mathrm{dc-1}}$. Each of the H-Bridges in the DC/DC conversion outputs a square-wave voltage. As a result, $u_{\mathrm{M-}i}$ (i=1, 2, 3, ... , Y) has two voltage levels, which are $+U_{\mathrm{dc-}i}$ and $-U_{\mathrm{dc-}i}$ (i=1, 2, 3, ... , Y).

$$\begin{cases}-u_{\mathrm{M-1}}+L_{\mathrm{T}}\dfrac{\mathrm{d}i_{\mathrm{T-1}}}{\mathrm{d}t}=-u_{\mathrm{M-1}}+L_{\mathrm{T}}\dfrac{\mathrm{d}i_{\mathrm{T-1}}}{\mathrm{d}t}\\ -u_{\mathrm{M-1}}+L_{\mathrm{T}}\dfrac{\mathrm{d}i_{\mathrm{T-1}}}{\mathrm{d}t}=-u_{\mathrm{M-2}}+L_{\mathrm{T}}\dfrac{\mathrm{d}i_{\mathrm{T-2}}}{\mathrm{d}t}\\ \cdots\cdots\\ -u_{\mathrm{M-1}}+L_{\mathrm{T}}\dfrac{\mathrm{d}i_{\mathrm{T-1}}}{\mathrm{d}t}=-u_{\mathrm{M-Y}}+L_{\mathrm{T}}\dfrac{\mathrm{d}i_{\mathrm{T-Y}}}{\mathrm{d}t}\end{cases} \tag{9}$$

Fig. 8 shows the equivalent circuit of the DC/DC conversion in the center of a PET. As shown in Fig. 3, Y is the number of H-Bridges connected with the high-frequency transformer. To simplify the analysis, the leakage inductors L_{T} of all the windings are assumed to be equal. From the equivalent circuit, (9) can be formed.

Add up all the equations in (9). Then, in Fig. 8, $i_{\mathrm{T-1}}+i_{\mathrm{T-2}}+\ldots+i_{\mathrm{T-}Y}=0$ can be obtained. Thus, after simplification, it is possible to obtain:

$$YL_{\mathrm{T}}\frac{di_{\mathrm{T-1}}}{dt}=\sum_{j=1}^{Y}(u_{\mathrm{M-1}}-u_{\mathrm{M-}j}) \tag{10}$$

Fig. 9 shows the equivalent circuit of (10), in which the currents are denoted by $i_{\mathrm{T-1-1}}\sim i_{\mathrm{T-1-}Y}$. Thus, $i_{\mathrm{T-1}}$ is:

$$i_{\mathrm{T-1}}=\sum_{j=1}^{Y}i_{\mathrm{T-1-}j} \tag{11}$$

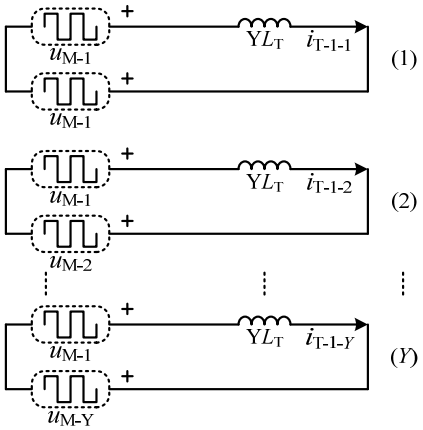

Fig. 9. Equivalent circuits for the entire system from equation (10).

The instantaneous power of u_{M-1}, shown in Fig. 8, is denoted by p_1, as shown in (12). Therefore, p_1 is the sum of all the instantaneous power of u_{M-1} in all of the equivalent circuits shown in Fig.9.

$$p_1 = u_{M-1} i_{T-1} = \sum_{j=1}^{Y} u_{M-1} i_{T-1-j} \tag{12}$$

The average power of each voltage source shown in Fig. 8 is denoted by P_1, P_2, ..., and P_Y. The average powers of u_{M-1} in Fig.9(1) ~ Fig.9(Y) are denoted by P_{1-1}, P_{1-2}, ... , and P_{1-Y}, respectively. Therefore, from (12), P_1 can be written as:

$$P_1 = \sum_{j=1}^{Y} P_{1-j} \tag{13}$$

In the steady state, all of the DC capacitor voltages are controlled to be U_{dc}. Thus, $U_{dc-1}=U_{dc-2}=...=U_{dc-Y}=U_{dc}$. Taking Fig. 9(2) as an example, the average power of u_{M-1} is denoted by P_{1-2} and can be obtained in (14).

$$P_{1-2} = \frac{U_{dc}^{\ 2}(\pi - |\theta_1 - \theta_2|)(\theta_1 - \theta_2)}{\pi \omega Y L_T} \tag{14}$$

In (14), U_{dc} is the voltage of every DC capacitor. ω demonstrates the angular frequency of all the voltage sources. θ_j is the phase of u_{M-j}(j=1,2, ... , Y). More importantly, $\theta_{jk} \equiv \theta_j - \theta_k$ (j=1,2, ... , Y; k=1, 2, ... , Y). In (14), $f(\theta_{jk}) \equiv (\pi - |\theta_1 - \theta_2|)(\theta_1 - \theta_2)$ can be replaced with the expression $e \times \sin(\theta_{12})$. The parameter e can be calculated as:

$$\min \int_{-\pi}^{\pi} [f(\theta_{12}) - e \times \sin(\theta_{12})]^2 d\theta_{12} \tag{15}$$

Therefore, it is possible to obtain:

$$e = \frac{8}{\pi} \tag{16}$$

Thus, the expression $(\pi - |\theta_{12}|)\theta_{12}$ in (14) can be substituted by $8\sin(\theta_{12})/\pi$ shown in (16). Fig. 10 shows the curves of the two functions, which demonstrates their similarity.

Since θ_{jk}(j=1, 2, 3, ... ,Y; k=1, 2, 3, ... ,Y) is small and around zero, $\sin(\theta_{jk}) \approx \theta_{jk}$. In addition, (14) can be simplified as:

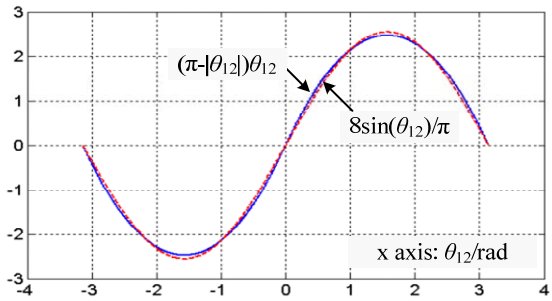

Fig. 10. Curves of $(\pi - |\theta_{12}|)\theta_{12}$ and $8\sin(\theta_{12})/\pi$.

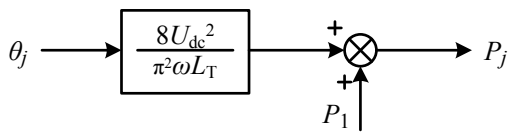

Fig. 11. Diagram from θ_j to P_j.

$$P_{1-2} = \frac{8U_{dc}^{\ 2}(\theta_1 - \theta_2)}{\pi^2 \omega Y L_T} \tag{17}$$

Therefore, the expression of P_{j-k} can be obtained as:

$$P_{j-k} = \frac{8U_{dc}^{\ 2}(\theta_j - \theta_k)}{\pi^2 \omega Y L_T} \tag{18}$$

From (13) and (18), P_j (j=1, 2, 3, ... ,Y) can be written as:

$$P_j = \frac{8U_{dc}^{\ 2}}{\pi^2 \omega Y L_T}\left(Y\theta_j - \sum_{k=1}^{Y} \theta_k\right) \tag{19}$$

As a result, the average power of all the voltage sources shown in Fig. 8 can be obtained as follows.

$$\begin{bmatrix} Y-1 & -1 & \dots & -1 \\ -1 & Y-1 & \dots & -1 \\ \dots & \dots & \dots & \dots \\ -1 & -1 & \dots & Y-1 \end{bmatrix} \begin{bmatrix} \theta_1 \\ \theta_2 \\ \dots \\ \theta_Y \end{bmatrix} = \frac{\pi^2 \omega Y L_T}{8U_{dc}^{\ 2}} \begin{bmatrix} P_1 \\ P_2 \\ \dots \\ P_Y \end{bmatrix} \tag{20}$$

Given that θ_1=0 and considering $P_1+P_2+...+P_Y \approx 0$, the solution of (20) is as (21), where j=2, 3, ... ,Y.

$$\theta_j = \frac{\pi^2 \omega L_T}{8U_{dc}^{\ 2}}(P_j - P_1) \Rightarrow P_j = \frac{8U_{dc}^{\ 2}\theta_j}{\pi^2 \omega L_T} + P_1 \tag{21}$$

Fig. 11 reveals the relationship between the phase and the average power for each voltage source in Fig. 8.

2) Control Diagram of the DC/DC Conversion

P_{load-j} (j=1, 2, 3, ... ,Y) is the average load power of U_{dc-j}. Therefore, the equations of the capacitor voltages can be written as:

$$\begin{cases} \dfrac{C_{dc-1}}{2}\dfrac{d(U_{dc-1}^{\ 2})}{dt} = P_1 - P_{load-1} \\ \dfrac{C_{dc-2}}{2}\dfrac{d(U_{dc-1}^{\ 2})}{dt} = P_2 - P_{load-2} \\ \cdots\cdots \\ \dfrac{C_{dc-Y}}{2}\dfrac{d(U_{dc-Y}^{\ 2})}{dt} = P_Y - P_{load-Y} \end{cases} \tag{22}$$

Fig. 12 shows the signal flow from P_j-P_{load-j} to θ_j, where

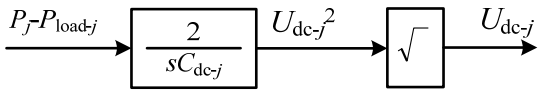

Fig. 12. Calculation diagram of $U_{dc\text{-}j}$.

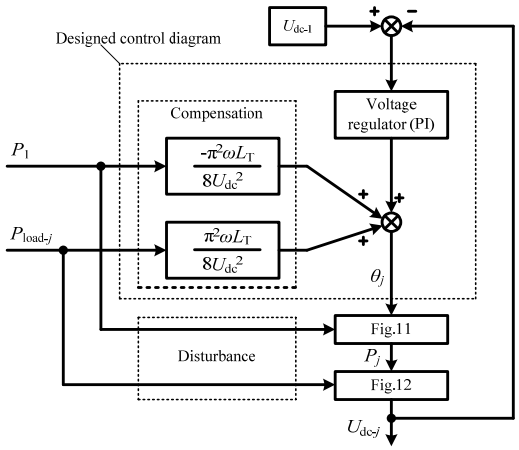

Fig. 13. Control diagram of DC/DC conversion.

j=1, 2, 3, ... ,Y. Thus, the capacitor voltage can be controlled by adjusting the value of P_j-$P_{load\text{-}j}$. This also means that $P_{load\text{-}j}$ can be treated as a disturbance of the capacitor voltage.

A control diagram of the DC/DC conversion is shown in Fig. 13. The reference voltage of $U_{dc\text{-}j}$ (j=2, 3, ... ,Y) is $U_{dc\text{-}1}$. The transfer function of the system is made up of three blocks. These blocks are a proportional block (Fig. 11), a delay block (because of the PWM) and an integration block (Fig. 12). Therefore, the transfer function is equivalent to the system in Fig. 6(a), and since it is in the steady state, the voltage reference is galvanic (the resonant angular frequency is zero), and a PI regulator is adopted. The regulator's output is θ_j, which changes $U_{dc\text{-}j}$ as shown in Fig. 11 and Fig. 12.

As shown in Fig. 13, there are two disturbances for $U_{dc\text{-}j}$, which are P_1 and $P_{load\text{-}j}$. Compensation paths are constructed to eliminate disturbances and to improve the performance.

3) Phase shifting for the DC/DC conversion

In order to maintain $U_{dc\text{-}j}$(j=2, 3, ... , Y), it is essential to adjust θ_j. This means shifting the phase of the square waveform. The modulation for the phase shifting is shown in Fig.14. The top axis frame depicts the curve of θ_j, which can be changed every T_T. The middle axis frame in Fig. 14 contains a virtual saw waveform, three boundary lines, and $F_{cnt}(\theta_j)$, which are all necessary to generate pulses for power electronic switches.

As shown in Fig. 14, the saw waveform rises from $F_{cnt}(\theta_j)$ to $F_{cnt}(\theta_j)+T_{T\text{-}cnt}$. Then it drops to $F_{cnt}(\theta_j)$ and is repeated. $T_{T\text{-}cnt}$, which is the maximum value of the saw waveform when the saw waveform begins at 0, is defined as (23). $F_{cnt}(\theta_j)$ is proportional to θ_j, as shown in (24).

$$T_{T-cnt} = \frac{T_T}{T_{tick}} \tag{23}$$

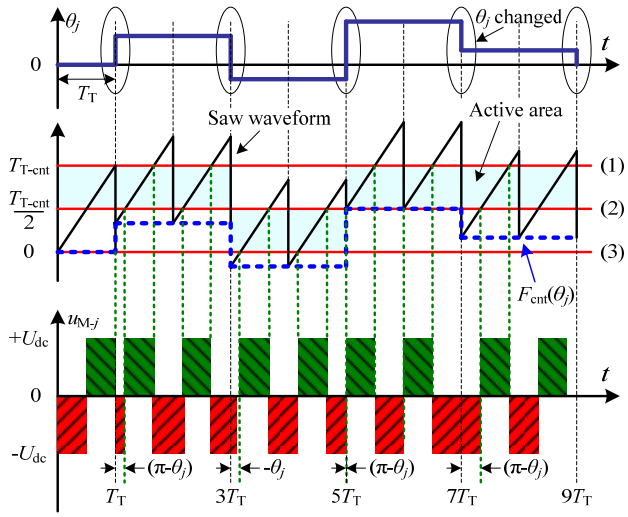

Fig. 14. Phase shifting scheme for DC/DC conversion. (Top) Curve of θ_j. (Middle) Saw curve and Fcnt(θ_j) to generate gate pluses. (Bottom) Output of H-Bridge.

$$F_{cnt}(\theta_j) = \frac{\theta_j T_T}{2\pi T_{tick}} \tag{24}$$

In (23) and (24), T_{tick} is the crystal period of the saw waveform. What should be pointed out is that in Fig. 10, θ_j is between -π and +π. However, in practical applications, L_T is designed to be small so that θ_j is around zero.

There are three boundaries on the axis frame, which are referred to as (1), (2) and (3) in the middle of Fig. 14. In addition, an active area is introduced to generate pulses. When $F_{cnt}(\theta_j)$ is positive, the active area is between boundary (1) and boundary (2). When $F_{cnt}(\theta_j)$ is not positive, the active area is between boundary (2) and boundary (3). The crossings in the active area determine the phase of the voltage. Thus, pulses can be generated.

4) Cascaded H-Bridge Inverter

All of the DC link voltages are controlled to be equal to $U_{dc\text{-}1}$ when in operation. In addition, the DC voltages are isolated from each other due to the DC/DC conversion.

As a PET, the secondary side is to output a reference voltage with the proper amplitude and frequency, and a low THD (Total Harmonic Distortion).

A low-pass second-order filter is used to generate a sinusoidal voltage. The capacitor voltage, which is also regarded as the output voltage and denoted by u_R, can be changed by the current i_{LR} on the inductor L_R in Fig.3. In addition, the current of the load also changes u_R.

Fig. 15 shows a model diagram and a control diagram of the CHB inverter. u_{inv} is the output of the CHB, and i_R is the load current. L_R is the output-side inductor. C_R is the capacitor on the output-side. The reference signals for voltage regulator and current regulator are both sinusoidal. Therefore, a PR regulator can be adopted. The analysis and discussions

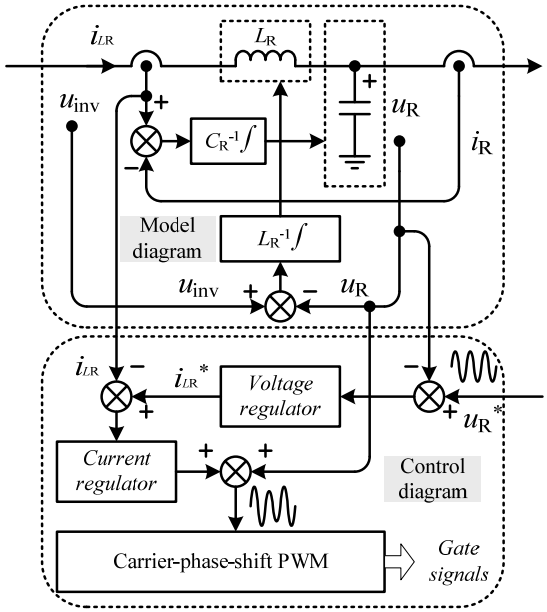

Fig. 15. Model and control diagram of CHB inverter with low-pass filter. (Top: model diagram for CHB inverter, Bottom: Control diagram including voltage loop and current loop).

about the control system are similar to those in sub-section *A*, section III. For three-phase output occasions, the d-q transform can be used to simplify the design of the control diagram.

IV. Experimental Results

A. Experimental System Configuration

In the laboratory, an experimental system is established to evaluate the proposed PET. The experimental system is based on the topology shown in Fig. 16. The CHB rectifier is made up of two H-Bridges, and the CHB inverter is also made up of two H-Bridges. There are four windings on the high-frequency transformer. In addition, the parameters of the experimental system are shown in TABLE I.

The experimental system is shown in Fig. 17. Element (1) is the power supply for all of the boards. Element (2) is a DSP controller (TMS320F28335), which is used to implement all of the algorithms. Element (3) is an EPM1270 CPLD, which is used for generating PWM signals, coding the PWM signals and processing data. Element (4) is made up of voltage sensors that are used to measure the grid voltages and DC capacitor voltages. Element (5) is made up of current sensors. Element (6) is a twisted wire for signal transfer. Element (7) is the inductor on the primary side. Element (8) is an EPM1270 CPLD for decoding serial signals and processing data. Element (9) is a power electronic switch (IRF640 MOSFET, 3 MOSFETs connected in parallel as a switch) with cooling devices. Element (10) is made up of DC capacitors. Element (11) is a 20kHz high-frequency transformer.

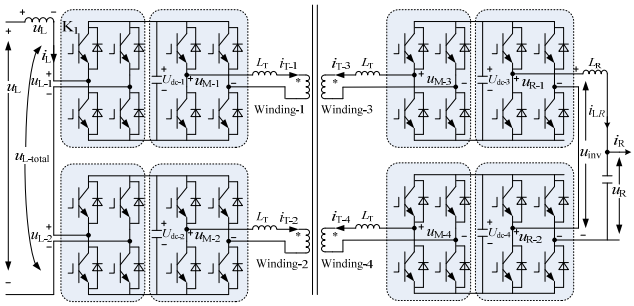

Fig. 16. Topology of experimental system for PET.

TABLE I
Experimental System Parameters

Input/output phases	sing-phase/single-phase
Power rating P	5kW
Capacitor Voltage $U_{dc-1} \sim U_{dc-4}$	80V
PWM Switching Frequency f_s	2kHz
Frequency of high-frequency isolation f_T	20kHz
Inductance on primary side L_L	1mH
Inductance on secondary side L_R	1mH
Capacitor on secondary side C_R	47uF×2
Leakage Inductance L_T	22uH
Number of windings Y	4
H-Bridge number of the CHB rectifier	2
H-Bridge number of the CHB inverter	2
Primary side voltage u_L	60sin(100πt)V
Secondary side voltage u_R	120sin(100πt)V
Load R_{load}	24Ω

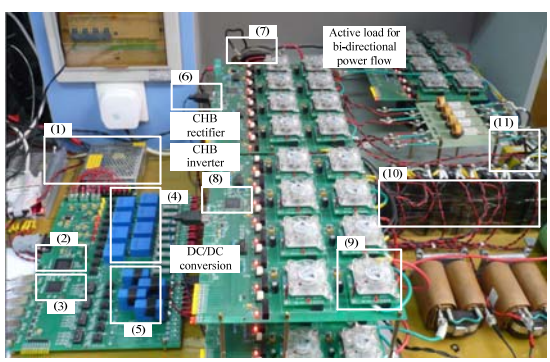

Fig. 17. Experimental system of the converter.

In Fig. 17, there are five power boards. Each board consists of two H-bridges. Two of the boards are for DC/DC conversion, one is for the CHB rectifier, one is for the CHB inverter and one is for the active load.

Fig. 18 shows every part of the control board. Element (1) ~ (4) are the voltage sensors for U_{dc-1}~U_{dc-4}. Element (5) ~ (6) are for u_L and u_R. Element (9) ~ (11) are for i_L, i_{LR} and i_R, respectively. Element (13) ~ (16) are serial signals used to drive the H-Bridges. Element (7), (8), (12) and (17) are for expansion.

As shown in Fig. 17 and Fig. 18, all of the PWM signals are encoded. Thus, one wire can carry all of the driving

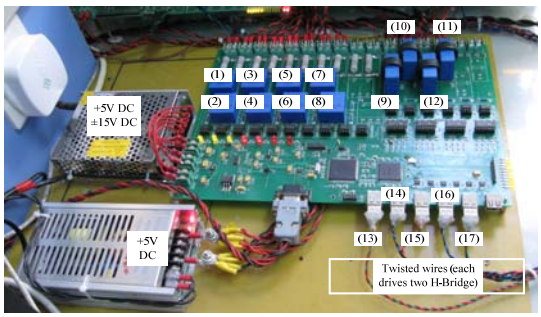

Fig. 18. Control board layout.

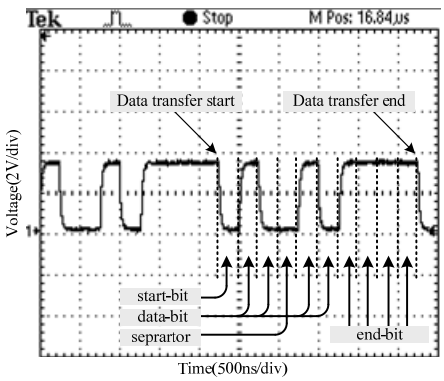

Fig. 19. Waveform of the serial signal.

pulses for every H-Bridge cell. Therefore, the reliability is improved and the number of wires between the control board and the power circuits is reduced.

Fig. 19 shows a waveform of one serial signal. One frame of the data lasts 250ns and the data begins with a drop in the voltage. The protocol is as follows: (1) the first 250ns is the start-bit; (2) the second, third, fifth and sixth 250ns are the data-bits which indicate the on/off states of the switches; (3) the fourth 250ns is the separator; (4) The last four 250ns are the stop-bit indicating the end of one frame.

B. Results Analysis

Fig. 20 shows experimental waveforms of u_L and i_L, which are both 50Hz sinusoidal AC signals. The power factor on the primary side of the PET is high and the reactive power is eliminated. i_L is sinusoidal, indicating that the THD is low.

Fig. 21 shows the voltage on L_L, which is an inductor as a filter on the primary side. In theory, it is equal to u_L-$u_{L\text{-total}}$.

The outputs of the two H-Bridges on the primary side are denoted by $u_{L\text{-}1}$ and $u_{L\text{-}2}$. Fig. 22 shows the waveforms of $u_{L\text{-}1}$, $u_{L\text{-}2}$ and $u_{L\text{-}1}$+$u_{L\text{-}2}$. $u_{L\text{-}1}$ and $u_{L\text{-}2}$ both have three levels, which are -80V, 0, and +80V. Because the reference values are equal, as shown in Fig.5, their fundamental components are the same. In addition, because of the phase-shift of the carriers, their sum, denoted by $u_{L\text{-}1}$+$u_{L\text{-}2}$, has five levels, which are -160V, -80V, 0, +80V, and +160V. Therefore, it can be inferred that $U_{dc\text{-}1}$ and $U_{dc\text{-}2}$ are both about 80V, which shows that the control algorithm of the CHB rectifier presented in this paper is effective.

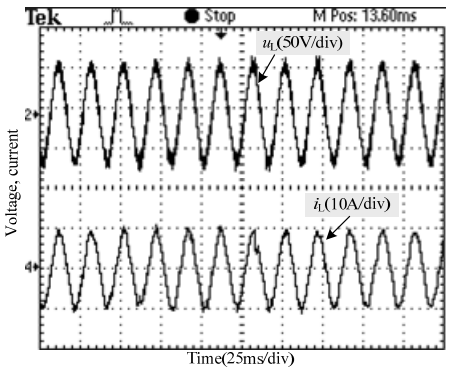

Fig. 20. Waveforms of primary input voltage and current. (Ch2) Primary side input voltage. (Chn4) Primary side input current.

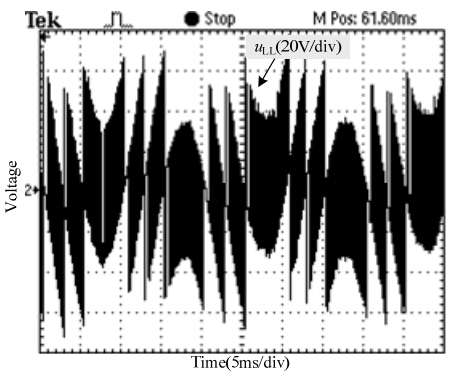

Fig. 21. Voltage on the primary side inductor.

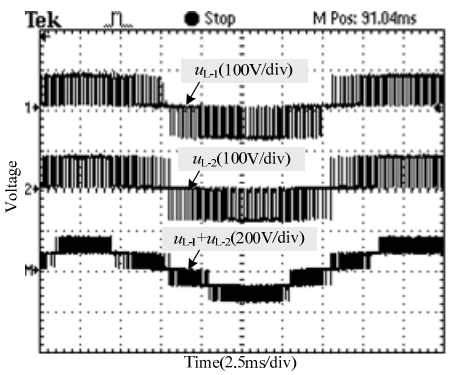

Fig. 22. Outputs of H-Bridges in CHB rectifier and their sum. (Ch1) Output of the first H-bridge in CHB rectifier. (Ch2) Output of the second H-bridge in CHB rectifier. (ChM) Sum of the two outputs in CHB rectifier.

After expanding Fig. 22, the waveforms in each switching period are shown in Fig. 23. The output voltage of each H-Bridge has three voltage levels. In addition, the fundamental voltages of $u_{L\text{-}1}$ and $u_{L\text{-}2}$ are equal. However, because of the differences in the carrier phases, their switching patterns are not the same. The time between the two rising edges of $u_{L\text{-}1}$ and $u_{L\text{-}2}$ is 250us, verifying that the switching frequency is 2kHz. The time between the first rising edges of $u_{L\text{-}1}$ and $u_{L\text{-}2}$ is 125us. Therefore, the difference between the two carriers is π/2. The time between the rising edges of $u_{L\text{-}1}$+$u_{L\text{-}2}$ is 125us. Thus, the equivalent

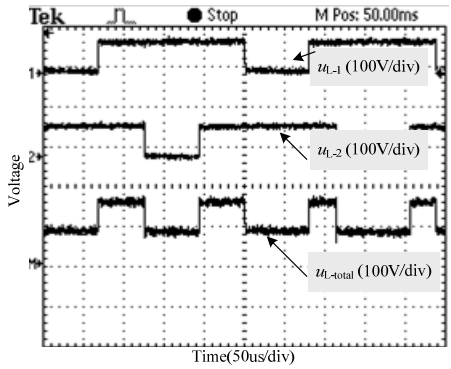

Fig. 23. Outputs of H-Bridges in CHB rectifier and their sum (expanded). (Ch1) Output of the first H-bridge in CHB rectifier. (Ch2) Output of the second H-bridge in CHB rectifier. (ChM) Sum of the two outputs in CHB rectifier.

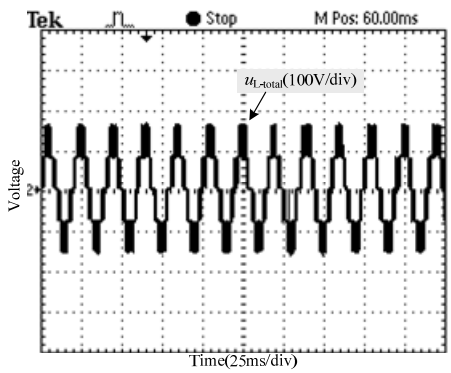

Fig. 24. Output of CHB rectifier.

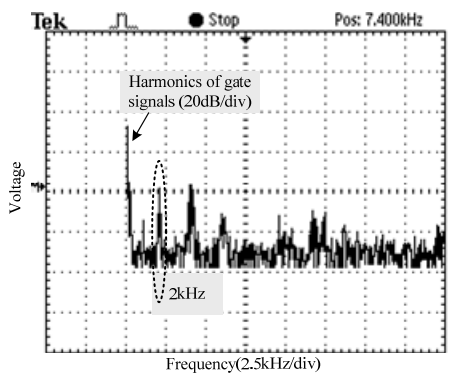

Fig. 25. Harmonics of the gate signal.

switching frequency is improved to 8kHz.

In the experimental system, the two H-Bridges are serialized together. u_{L-1}+u_{L-2} is the theoretical value of $u_{L-total}$. Fig. 24 shows the waveform of $u_{L-total}$.

As shown in Table I, the switching frequency of each H-Bridge in the rectifier is 2kHz. The harmonics of the gate signal for K_1 in Fig. 16 are shown in Fig.25. The frequency of the dominant harmonic is 2kHz.

By shifting the phases of the carriers, the equivalent switching frequency is increased. Fig. 26 shows the harmonics of $u_{L-total}$, which in theory is the sum of u_{L-1} and u_{L-2}. The spectrum shows that the dominant harmonics are

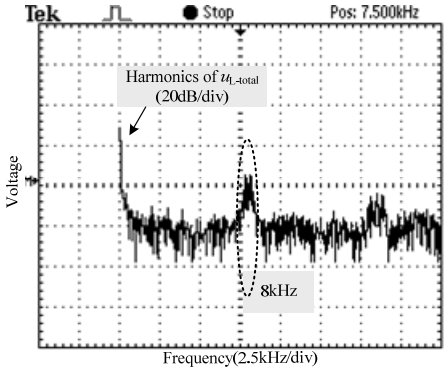

Fig. 26. Harmonics of CHB rectifier output.

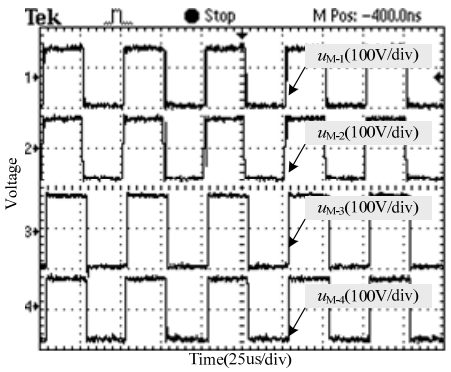

Fig. 27. Four input voltages on the windings of high-frequency transformer in DC/DC conversion. (Ch1) Output of H-Bridge connected with windings-1. (Ch2) Output of H-Bridge connected with windings-2. (Ch3) Output of H-Bridge connected with windings-3. (Ch4) Output of H-Bridge connected with windings-4.

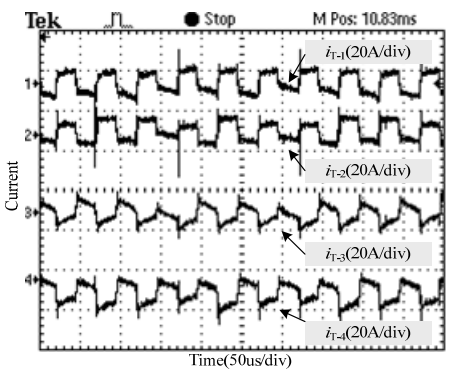

Fig. 28. Four input currents flowing into high-frequency transformer in DC/DC conversion. (Ch1) Current flows into windings-1. (Ch2) Current flows into windings-2. (Ch3) Current flows into windings-3. (Ch4) Current flows into windings-4.

near 8kHz. Thus, the THD is reduced and the equivalent switching frequency is increased. Hence, the characteristics of i_L are improved because of the low THD.

Fig. 27 shows the waveforms of u_{M-1}, u_{M-2}, u_{M-3}, and u_{M-4}. The four voltages are all square waveforms and the frequency is 20kHz. The phase of u_{M-1} is almost the same as that of u_{M-2}. That is because the two H-Bridges of the rectifier share almost the same load. Similarly, the phases of u_{M-3} and u_{M-4} are almost

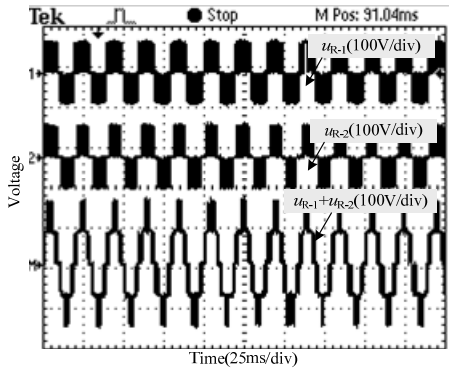

Fig. 29. Outputs of H-Bridges in CHB rectifier and their sum. (Ch1) Output of the first H-Bridge in CHB inverter. (Ch2) Output of the second H-Bridge in CHB inverter. (Ch3) Sum of the two outputs in CHB inverter.

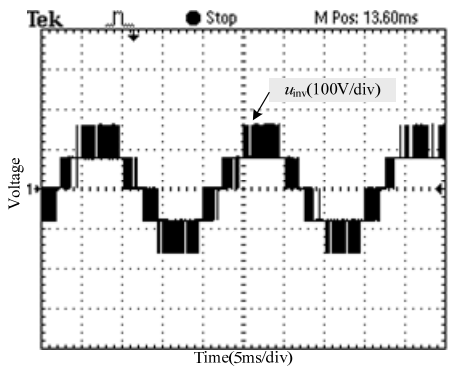

Fig. 30. Outputs of CHB inverter.

the same. Since the phase of u_{M-1}(u_{M-2}) is ahead of that of u_{M-3}(u_{M-4}), according to (18), the power flows from the primary side to the secondary side.

Fig. 28 shows the four currents flowing into the windings of the transformer. The four currents are denoted by $i_{T-1} \sim i_{T-4}$. The phase of i_{T-1} is ahead of the phase of i_{T-3} by approximately π. In addition, as shown in Fig. 27, the phases of $u_{T-1} \sim u_{T-4}$ are similar. Therefore, the power from $u_{T1} \sim u_{T-2}$ to the windings is positive, while the power from $u_{T-3} \sim u_{T-4}$ to the windings is negative.

Fig. 29 shows the output of the two H-Bridges in the CHB inverter. The voltages are denoted by u_{R-1} and u_{R-2}, and their sum is also shown in Fig. 29. Like the CHB rectifier, the output of each H-Bridge has three voltage levels which are -80V, 0, and +80V. Because of the shifted carrier-phase, their sum has five voltage levels.

Fig. 30 shows a waveform of u_{inv}, which is the output of the CHB inverter. In theory, u_{inv} has five voltage levels. Every voltage step is 80V. This indicates that the voltages of the DC capacitors are 80V.

The low-pass filter is made up of L_R and C_R in Fig. 16, and most of the harmonics in u_{inv} are eliminated. Then the voltage u_R on the secondary side is shown in Fig. 31, which is sinusoidal. The frequency of u_R is 50Hz, and the amplitude of u_R is 120V.

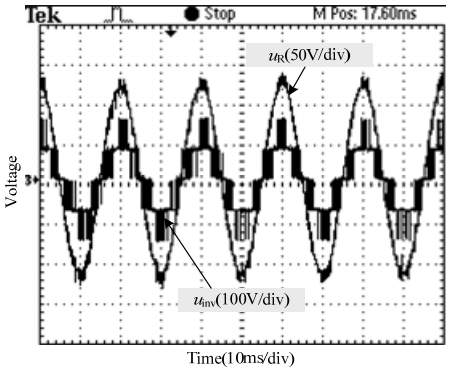

Fig. 31. Voltage and current on secondary side. (Ch1) Output voltage of CHB inverter. (Chn3) Output voltage on the secondary side.

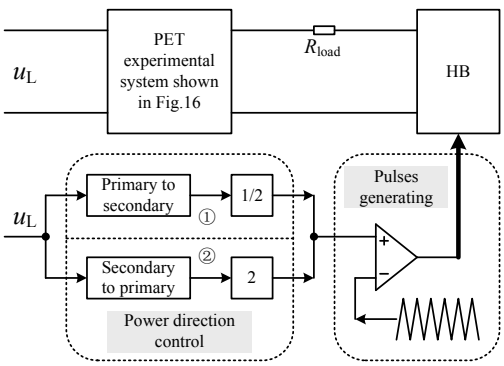

Fig. 32. Experimental system to verify bi-directional power flow ability.

C. *Bi-directional power-flow*

In order to verify the bi-directional power-flow ability, another inverter is used to build an active load for the PET. The experimental system for a bi-directional power-flow is shown in Fig. 32. When mode ① (the upper path) is activated, the current can be written as (25). When mode ② (the lower path) is activated, the current can be written as (26).

$$i_R = \frac{u_R - \frac{1}{2}u_R}{R_{load}} = \frac{u_R}{2R_{load}} \tag{25}$$

$$i_R = \frac{u_R - \frac{3}{2}u_R}{R_{load}} = -\frac{u_R}{2R_{load}} \tag{26}$$

From (25), it can be concluded that the phases of i_R and u_R are the same. Therefore, the power is from the primary side to the secondary side. Meanwhile, in (26) i_R/u_R is negative. Therefore, the power flows from the secondary side to the primary side.

Fig. 33 shows the voltage and current on the primary side. In the beginning, the power flows from the primary side to the right side. The phases of the voltage and the current are the same. Then the system switches to mode ②. Then the power flows reversely, that is, from the secondary side to the primary side. The DC capacitor voltages of the CHB inverter

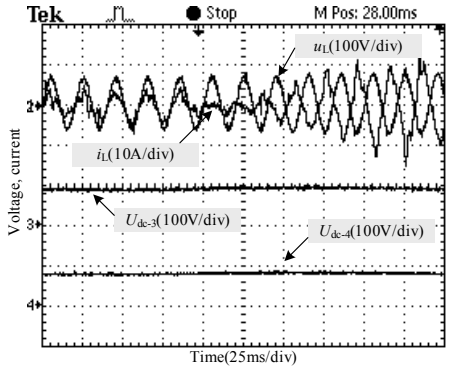

Fig. 33. Transient waveform when power flows from primary side to secondary side. (Chn1) Primary side input voltage. (Ch2) Primary side input current. (Ch3) The first DC capacitor voltage in CHB inverter. (Ch4) The second DC capacitor voltage in CHB inverter.

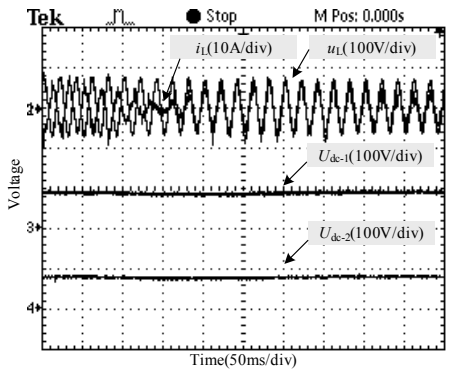

Fig. 34. Transient waveform when power flows from secondary side to primary side. (Chn1) Primary side input voltage. (Ch2) Primary side input current. (Ch3) The first DC capacitor voltage in CHB rectifier. (Ch4) The second DC capacitor voltage in CHB rectifier.

are also shown in Fig. 33. During this process, U_{dc-3} and U_{dc-4} are both 80V, indicating that the scheme is practical and that the power is under control. Another operation is shown in Fig. 34. This operation is from mode ② to mode ①. The DC capacitor voltages in the CHB rectifier are both 80V.

Hence, the PET can work in the bi-directional power-flow mode, which is necessary for the transformers in power systems.

D. System efficiency measurement

With the parameters shown in TABLE I, the system efficiency is measured by changing the current on the load, which has a resistance of 24Ω.

The experimental data is shown in TABLE II. The maximum load current is 6.3A. The resistance can be measured precisely. As a result, the output power can be calculated. In addition, since the input power factor is approximately 1 and the input voltage is known, the input power can also be calculated.

The system efficiency curve shown in TABLE II is drawn in Fig. 35.

TABLE II
RESULTS OF THE SYSTEM EFFICIENCY

Amplitude of i_R (A)	Amplitude of i_L (A)	Power input (W)	Power output(W)	Efficiency (%)
2.5	3.4	102	75	73.5
3.1	4.5	135	115	85.4
3.8	6.9	207	173	83.7
4.4	9.1	273	232	85.1
5.1	12.1	363	312	86.0
5.7	15.7	471	390	82.8
6.3	19.8	591	476	80.6

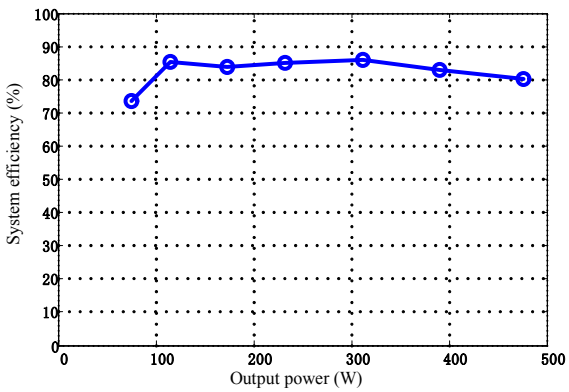

Fig. 35. Curve of the system efficiency.

TABLE III
RESULTS OF THE POWER MEASURED FOR THE SUB-PARTS

Sub-part name	Power in (W)	Power out (W)	Power loss(W)	Sub-part Efficiency (%)
CHB rectifier	591	552	39	93.4
DC/DC Conv.	552	509	43	92.2
CHB inverter	509	476	33	93.5

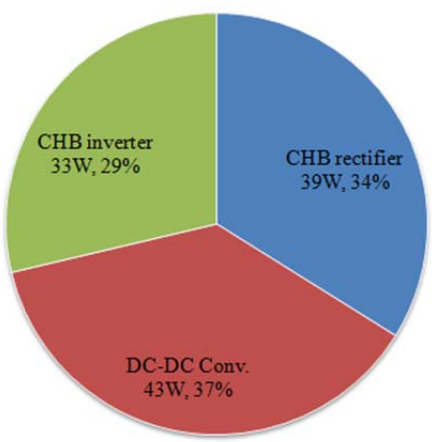

Fig. 36. Power loss and percentages of sub-parts.

The power flowing into and out of the three sub-parts introduced in section III was also measured when the output

power was 476W, as shown in TABLE II, and the results are listed in TABLE III.

As shown in TABLE III, the power losses for the three sub-parts are very close. Advanced MOSFETs with a lower R_{DS} and better switching performance can be adopted to reduce the power loss and improve the efficiency.

Fig. 36 shows the power losses and percentages of the three sub-parts. The power loss in the DC-DC Conversion is the greatest. However, because the current on each switch is much smaller than that in the other two sub-parts, which can significantly reduce the conductive loss, the power loss is 43W. This is a little more than the power loss in the other two sub-parts.

V. CONCLUSION

In this paper, a topology for a PET which may be able to replace the traditional transformers in power systems is proposed. The proposed PET consists of three parts and each part is based on an H-bridge, which is highly modularized. HF isolation is applied to decrease the size and weight of the system. Because of its cascaded structure, the PET can output multilevel high voltages. As a result, it can be connected with a high voltage power grid directly. The proposed PET is flexible because it has active control on both sides. By changing the reference value, the turn ratio of the transformer can be changed on-grid. This characteristic is valuable for voltage regulation in power systems.

The control algorithm of the proposed PET is discussed in great detail in this paper, including the DC capacitor voltage maintenance in the CHB rectifier, and the power flow control in the DC/DC conversion. The general control strategy is as follows: (1) The CHB rectifier aims to keep the sum of all the DC capacitor voltages in the CHB rectifier constant; (2) The DC/DC conversion is used to keep all the DC capacitor voltages equal.

An experimental prototype is built to validate the proposed topology and control algorithm. The results demonstrate that the proposed PET is practical and that the control algorithm is effective. The PET can output a multilevel high voltage, and the voltage on the secondary side can be sinusoidal. In addition, the frequency and amplitude of the voltage on the secondary side can be changed as desired. This makes it possible to change the turn ratio without an interrupt which makes the power system more flexible and reliable.

An extra inverter is designed to verify the ability of bi-directional power-flow, since this is essential in some applications, such as renewable resource generation, HVDC and smart power flow regulation.

The system efficiency is measured (86% overall, and 93.4%, 92.2%, 93.5%, separately). The efficiency can be improved with new types of semi-conductor switches and materials.

ACKNOWLEDGMENT

This research work was supported by National Natural Science Foundation of China (51207010).

REFERENCES

[1] C. Chakraborty, H. Iu, and D. Lu, "Power converters, control, and energy management for distributed generation," *IEEE Trans. Ind. Electron.*, Vol. 62, No. 7, pp. 4466-4470, Jul. 2015.

[2] S. Alepuz, A. Calle, S. B. Monge, S. Kouro, and B. Wu, "Use of stored energy in PMSG rotor inertia for low-voltage ride-through in back-to-back NPC converter-based wind power systems," *IEEE Trans. Ind. Electron.*, Vol. 60, No. 5, pp. 1787-1796, May 2013.

[3] S. Mehraeen, S. Jagannathan, and M. L. Crow, "Novel dynamic representation and control of power systems with FACTS devices," *IEEE Trans. Power Syst.*, Vol. 25, No. 3, pp. 1542-1554, Aug. 2010.

[4] J. M. Carrasco, L. G. Franquelo, J. T. Bialasiewicz, E. Galvan, C. Ramon, P. Guisado, M. A. M. Prats, J. I. Leon, and N. M. Alfonso, "Power-electronic systems for the grid integration of renewable energy sources: a survey," *IEEE Trans. Ind. Electron.*, Vol. 53, No. 4, pp. 1002-1016, Jun. 2006.

[5] N. Johansson, L. Angquist, and H.-P. Nee, "An adaptive controller for power system stability improvement and power flow control by means of a thyristor switched series capacitor (TSSC)," *IEEE Trans. Power Syst.*, Vol. 25, No. 1, pp. 381-391, Feb. 2010.

[6] G. Franceschini, E. Lorenzani, and G. Buticchi, "Saturation compensation strategy for grid connected converters based on line frequency transformers," *IEEE Trans. Energy Convers.*, Vol. 27, No. 2, pp. 229-237, Jun. 2012.

[7] S. Roy and L. Umanand, "Integrated magnetics-based multisource quality ac power supply," *IEEE Trans. Ind. Electron.*, Vol. 58, No. 4, pp. 1350-1358, Apr. 2011.

[8] P. K. Jain, J. R. Espinoza, and H. Jin, "Performance of a single-stage UPS system for single-phase trapezoidal-shaped ac-voltage supplies," *IEEE Trans. Power Electron.*, Vol. 13, No. 5, pp. 912-923, Sep. 1998.

[9] H. Fan and H. Li, "High-frequency transformer isolated bidirectional DC–DC converter modules with high efficiency over wide load range for 20 kVA solid-state transformer," *IEEE Trans. Power Electron.*, Vol. 26, No. 12, pp. 3599-3608, Dec. 2011.

[10] T. Zhao, G. Wang, S. Bhattacharya, and A. Q. Huang, "Voltage and power balance control for a cascaded H-bridge converter-based solid-state transformer," *IEEE Trans. Power Electron.*, Vol. 28, No. 4, pp. 1523-1532, Apr. 2013.

[11] L. Jia and S. K. Mazumder, "A loss-mitigating scheme for dc/pulsating-dc converter of a high-frequency-link system," *IEEE Trans. Ind. Electron*, Vol. 59, No. 12, pp. 4537-4544, Dec. 2012.

[12] J. S. Lai and D. J. Nelson, "Energy management power converters in hybrid electric and fuel cell vehicles," *Proc. IEEE.*, Vol. 95, No. 4, pp. 766-777, Apr. 2007.

[13] H. S. h. Chung, W. L. Cheung, and K. S. Tang, "A ZCS bidirectional flyback dc/dc converter," *IEEE Trans. Power Electron.*, Vol. 19, No. 6, pp. 1426-1434, Nov. 2004.

[14] D. M. Bellur and M. K. Kazimierczuk, "Isolated

two-transistor zeta converter with reduced transistor voltage," *IEEE Trans. Circuits Syst. II, Exp. Briefs*, Vol. 58, No. 1, pp. 41-45, Jan. 2011.

[15] H. Xiao and S. Xie, "A ZVS bidirectional dc-dc converter with phase-shift pulse PWM control scheme," *IEEE Trans. Power Electron.*, Vol. 23, No. 2, pp. 813-823, Mar. 2008.

[16] S. Inoue and H. Akagi, "A bidirectional isolated dc-dc converter as a core circuit of the next-generation medium-voltage power conversion system," in *37th IEEE Power Electronics Specialists Conference(PESC),* pp. 1-7, Mar. Jun. 2006.

[17] J. Biela, M. Schweizer, S. Waffler, and J. W. Kolar, "SiC versus Si-Evaluation of potentials for performance improvement of inverter and dc-dc converter systems by SiC power semiconductors," *IEEE Trans. Ind. Electron.*, Vol. 58, No. 7, pp. 2872–2882, Jul. 2011.

[18] C. Mi, H. Bai, C. Wang, and S. Gargies, "Operation, design and control of dual H-bridge-based isolated bidirectional dc-dc converter," *IET Power Electron.* , Vol. 1, No. 4, pp. 507–517, Dec. 2008.

[19] G. G. Oggier, M. Ordonez, J. M. Galvez, and F. Luchino, "Fast transient boundary control and steady-state operation of the dual active bridge converter using the natural switching surface," *IEEE Trans. Power Electron.*, Vol. 29, No. 2, pp. 946–957, Feb. 2014.

[20] H. Bai and C. Mi, "Eliminate reactive power and increase system effi-ciency of isolated bidirectional dual-active-bridge DC-DC converters using novel dual-phase-shift control," *IEEE Trans. Power Electron.*, Vol. 23, No. 6, pp. 2905–2914, Nov. 2008.

[21] Y. Xie, J. Sun, and J. S. Freudenberg, "Power flow characterization of a bidirectional galvanically isolated high-power dc-dc converter over a wide operating range," *IEEE Trans. Power Electron.*, Vol. 25, No. 1, pp. 54–66, Jan. 2010.

[22] H. Bai, Z. Nie, and C. Mi, "Experimental comparision of traditional phase-shift,dual-phase-shift, and model-based control of isolated bidi-rectional dc-dc converters," *IEEE Trans. Power Electron.* , Vol. 25, No. 6, pp. 1444–1449, Jun. 2010.

[23] M. Sabahi, A. Y. Goharrizi, S. H. Hosseini, M. B. B. Sharifian, and G. B. Gharehpetian, "Flexible power electronic transformer," *IEEE Trans. Power Electron.*, Vol. 25, No. 8, pp. 2159-2169, Aug. 2010.

[24] M. Sabahi, S. H. Hosseini, M. B. B. Sharifian, A. Y. Goharrizi, and G. B. Gharehpetian, "A three-phase dimmable lighting system using a bidirectional power electronic transformer," *IEEE Trans. Power Electron.*, Vol. 24, No. 3, pp. 830-837, Mar. 2009.

[25] D. Dujic, F. Kieferndorf, F. Canales, and U. Drofenik, "Power electronic traction transformer technology - an overview," in *7th International Power Electronics and Motion Control Conference(IPEMC)*, Vol. 1, pp. 636-642, Jun. 2012.

[26] M. Malinowski, K. Gopakumar, J. Rodriguez, and M. A. Perez, "A survey on cascaded multilevel inverters," *IEEE Trans. Ind. Electron.*, Vol. 57, No. 7, pp. 2197-2207, Jul. 2010.

[27] J. D. Barros and J. F. Silva, "Multilevel optimal predictive dynamic voltage restorer," *IEEE Trans. Ind. Electron.*, Vol. 57, No. 8, pp. 2747-2760, Aug. 2010.

[28] S. Kouro, M. Malinowski, K. Gopakumar, J. Pou, L. G. Franquelo, B. Wu, J. Rodriguez, M. A. Perez, and J. I. Leon. "Recent advances and industrial applications of multilevel converters," *IEEE Trans. Ind. Electron*., Vol. 57, No. 8, pp. 2553-2580, Aug. 2010.

[29] Z. Du, L. M. Tolbert, and J. N. Chiasson, "Active harmonic elimination for multilevel converters," *IEEE Trans. Power Electron.*, Vol. 21, No. 2, pp. 459-469, Mar. 2006.

[30] C. R. Baier, J. R. Espinoza, J. A. Munoz, L. A. Moran, and P. E. Melin, "A high-performance multicell topology based on single-phase power cells for three-phase systems operating under unbalanced AC mains and asymmetrical loads," *IEEE Trans. Ind. Electron.*, Vol. 57, No. 8, pp. 2730-2738, Aug. 2010.

[31] H. Akagi, "Classification, terminology, and application of the modular multilevel cascade converter (MMCC)," *IEEE Trans. Power Electron.*, Vol. 26, No. 11, pp. 3119-3130, Nov. 2011.

[32] F. H. Khan, L. M. Tolbert, and W. E. Webb, "Hybrid electric vehicle power management solutions based on isolated and nonisolated configurations of multilevel modular capacitor-clamped converter," *IEEE Trans. Ind. Electron.*, Vol. 56, No. 8, pp. 3079-3095, Aug. 2009.

[33] F. Khoucha, S. M. Lagoun, K. Marouani, A. Kheloui, and M. E. H. Benbouzid, "Hybrid cascaded H-bridge multilevel-inverter induction-motor-drive direct torque control for automotive applications," *IEEE Trans. Ind. Electron.*, Vol. 57, No. 3, pp. 892-899, Mar. 2010.

[34] S. Lu and K. A. Corzine, "Advanced control and analysis of cascaded multilevel converters based on P-Q compensation," *IEEE Trans. Power Electron.*, Vol. 22, No. 4, pp. 1242-1252, Jul. 2007.

[35] N. Hatti, K. Hasegawa, and H. Akagi, "A 6.6-kV transformerless motor drive using a five-level diode-clamped PWM inverter for energy savings of pumps and blowers," *IEEE Trans. Power Electron.*, Vol. 24, No. 3, pp. 796-803, Mar. 2009.

[36] Y. Cheng, C. Qian, M. L. Crow, S. Pekarek, and S. Atcitty, "A comparison of diode-clamped and cascaded multilevel converters for a STATCOM with energy storage," *IEEE Trans. Ind. Electron.*, Vol. 53, No. 5, pp. 1512-1521, Oct. 2006.

[37] D. Krug, S. Bernet, S. S. Frazel, K. Jalili, and M. Malinowski, "Comparison of 2.3-kV medium-voltage multilevel converters for industrial medium-voltage drives," *IEEE Trans. Ind. Electron.*, Vol. 54, No. 6, pp. 2979-2992, Dec. 2007.

[38] P. Flores, J. Dixon, M. Ortuzar, R. Carmi, P. Barriuso, and L. Moran, "Static var compensator and active power filter with power injection capability, using 27-level inverters and photovoltaic cells," *IEEE Trans. Ind. Electron.*, Vol. 56, No. 1, pp. 130-138, Jan. 2009.

[39] J. I. Leon, S. Kouro, S. Vazquez, R. Portillo, L. G. Franquelo, J. M. Carrasco, and J. Rodriguez, "Multidimensional modulation technique for cascaded multilevel converters," *IEEE Trans. Ind. Electron.*, Vol. 58, No. 2, pp. 412-420, Feb. 2011.

[40] R. H. Baker and L. H. Bannister. "*Electric power converter*," U.S. Patent 3867643, Feb. 1975.

[41] J. Rodriguez, L. Moran, J. Pontt, P. Correa, and C. Silva, "A high-performance vector control of an 11-level inverter," *IEEE Trans. Ind. Electron.*, Vol. 50, No. 1, pp. 80-85, Feb. 2003.

[42] J. S. Lai and F. Peng, "Multilevel converters—a new breed of power converter," *IEEE Trans. Ind. Appl.*., Vol. 32, No. 3, pp. 509–517, May/Jun. 1996.

[43] X. Kou, K. A. Corzine, and M. W. Wielebski, "Overdistention operation of cascaded multilevel inverters,"

IEEE Trans. Ind. Appl., Vol. 42, No. 3, pp. 817-824, May/Jun. 2006.

[44] Z. Du, B. Ozpineci, L. M. Tolbert, and J. N. Chiasson, "DC-AC cascaded h-bridge multilevel boost inverter with no inductors for electric/hybrid electric vehicle applications," *IEEE Trans. Ind. Appl.*, Vol. 45, No. 3, pp. 963-970, May/Jun. 2009.

[45] P. Lezana and G. Ortiz, "Extended operation of cascade multicell converters under fault condition," *IEEE Trans. Ind. Electron.*, Vol. 56, No. 7, pp. 2697-2703, Jul. 2009.

[46] A. Nami, F. Zare, A. Ghosh, and F. Blaabjerg, "A hybrid cascade converter topology with series-connected symmetrical and asymmetrical diode-clamped H-bridge cells," *IEEE Trans. Power Electron.*, Vol. 26, No. 1, pp. 51-65, Jan. 2011.

[47] J. Rodriguez, L. Moran, J. Pontt, J. L. Hernandez, L. Silva, C. Silva, and P. Lezana, "High-voltage multilevel converter with regeneration capability," *IEEE Trans. Ind. Electron.*, Vol. 49, No. 4, pp. 839-846, Aug. 2002.

[48] P. Lezana, J. Rodriguez, and D. A. Oyarzun, "Cascaded multilevel inverter with regeneration capability and reduced number of switches," *IEEE Trans. Ind. Electron*., Vol. 55, No. 3, pp. 1059-1066, Mar. 2008.

[49] A. Dell'Aquila, M. Liserre, V. G. Monopoli, and C. Cecati, "Design of a back-to-back multilevel induction motor drive for traction systems," in *IEEE 34th Annual Power Electronics Specialist Conference,* Vol. 4, pp. 1764-1769, Jun. 2003.

[50] S. Vazquez, J. I. Leon, J. M. Carrasco, L. G. Franquelo, E. Galvan, M. Reyes, J. A. Sanchez, and E. Dominguez, "Analysis of the power balance in the cells of a multilevel cascaded H-bridge converter," *IEEE Trans. Ind. Electron.*, Vol. 57, No. 7, pp. 2287-2296, Jul. 2010.

[51] M. Hagiwara, K. Nishimura, and H. Akagi, "A medium-voltage motor drive with a modular multilevel PWM inverter," *IEEE Trans. Power Electron.*, Vol. 25, No. 7, pp. 1786-1799, Jul. 2010.

[52] H. AKagi and R. Kitada, "Control and design of a modular multilevel cascade BTB system using bidirectional isolated DC/DC converters," *IEEE Trans. Power Electron*., Vol. 26, No. 9, pp. 2457-2464, Sep. 2011.

[53] J. Shi, W. Gou, H. Yuan, T. Zhao, and A. Q. Huang, "Research on voltage and power balance control for cascaded modular solid-state transformer," *IEEE Trans. Power Electron.*, Vol. 26, No. 4, pp. 1154-1166, Apr. 2011.

[54] S. V. Araujo, P. Zacharias, and R. Mallwitz, "Highly efficient single-phase transformerless inverters for grid-connected photovoltaic systems," *IEEE Trans. Ind. Electron.*, Vol. 57, No. 9, pp. 3118-3128, Sep. 2010.

[55] Y. Hinago and H. Koizumi, "A single-phase multilevel inverter using switched series/parallel DC voltage sources," *IEEE Trans. Ind. Electron.*, Vol. 57, No. 8, pp. 2643-2650, Aug. 2010.

[56] E. Villanueva, P. Correa, J. Rodriguez, and M. Pacas, "Control of a single-phase cascaded H-bridge multilevel inverter for grid-connected photovoltaic systems," *IEEE Trans. Ind. Electron.*, Vol. 56, No. 11, pp. 4399-4406, Nov. 2009.

[57] S. Inoue and H. Akagi, "A bidirectional DC-DC converter for an energy storage system with galvanic isolation," *IEEE Trans. Power Electron.*, Vol. 22, No. 6, pp. 2299-2306, Nov. 2007.

[58] T. Jimichi, H. Fujita, and H. Akagi, "A dynamic voltage restorer equipped with a high-frequency isolated DC-DC converter," *IEEE Trans. Ind. Appl.*, Vol. 47, No. 1, pp.169-175, Jan./Feb. 2011.

[59] G. Shen, X. Zhu, J. M. Zhang, and D. Xu, "A new feedback method for PR current control of LCL-filter-based grid-connected inverter," *IEEE Trans. Ind. Electron.*, Vol. 57, No. 6, pp. 2033-2041, Jun. 2010.

[60] A. G. Yepes, F. D. Freijedo, O. Lopez, and J. D. Gandoy, "Analysis and design of resonant current controllers for voltage-source converters by means of nyquist diagrams and sensitivity function," *IEEE Trans. Ind. Electron.*, Vol. 58, No. 11, pp. 5231-5250, Nov. 2011.

Zhigang Gao was born in Hebei Province, China. He received his B.S. degree from Tianjin University, Tianjin, China, in 2005; his M.S. degree in Electrical Engineering from the Institute of Electrical Engineering, Chinese Academy of Sciences, Beijing, China, in 2008; and his Ph.D. degree in Electrical Engineering from Tsinghua University, Beijing, China, in 2011. In 2011, he joined the School of Automation, Beijing Institute of Technology, Beijing, China, where he is presently working as a Lecturer. His current research interests include power systems, multilevel converters, motor drives and renewable resource generation.

Hui Fan was born in Shanxi Province, China. He received his B.S. degree in Electrical Engineering from the Beijing Institute of Technology, Beijing, China, in 2013; where he is presently working towards his M.S. degree in Electrical Engineering. His current research interests include Z-source converters and energy storage systems.